Journal of Materials Chemistry C

ROYAL SOCIETY OF CHEMISTRY

PAPER

View Article Online
View Journal | View Issue

Cite this: J. Mater. Chem. C, 2021, 9, 584

The frequency-response behaviour of flexible piezoelectric devices for detecting the magnitude and loading rate of stimuli†

Ye Qiu,[ab] Shenshen Sun,[ab] Cong Xu,[ab] Youyan Wang,[ab] Ye Tian,*[ab] Aiping Liu,*[c] Xu Hou,[d] Hao Chai,[e] Zheng Zhang[ab] and Huaping Wu*[ab]

Received 22nd June 2020,
Accepted 16th August 2020

DOI: 10.1039/d0tc02949a

rsc.li/materials-c

Piezoelectric sensors with good flexibility and high sensitivity have attracted extensive interest in wearable electronics. Here, we report a novel frequency-response behaviour of piezoelectric voltage of a sensor that is based on a piezoelectric enhanced composite film of P(VDF-TrFE) and $BaTiO_3$. The piezoelectric voltage enhances with the increase of frequency and becomes stable beyond the critical frequency. Such a demonstrated sensing characteristic of the piezoelectric sensor depends on the inner resistance of the voltmeter, which is determined by whether the loading of stimuli can be completed within the period of piezoelectric voltage measurement in the testing circuit. By utilizing the frequency-response behaviour in different frequency ranges, the flexible piezoelectric device exhibits excellent capabilities to quantitatively detect the magnitude and loading rate of stimuli. As a proof-of-concept demonstration, a flexible pressure sensor is successfully integrated with a bionic bee to monitor the flight status (*i.e.*, strain rate and strain) of the vibrating wings. This work demonstrates that flexible piezoelectric sensors have great prospects for application in the field of bionic flying robots, thus paving the way forward for the development of smart self-sensing flexible electronics.

1. Introduction

An emerging development trajectory in wearable flexible electronics has received much attention due to their potential functions in intelligent robotics, healthcare monitoring, and medical diagnosis.[1–15] Tremendous efforts on developing flexible piezoelectric sensors with a high piezoelectric coefficient, excellent structural flexibility, and good mechanical robustness are reported. By virtue of their capability to convert mechanical stimuli into an electrical signal, piezoelectric sensors demonstrate wide applicability in measuring dynamic stimuli, such as vibrations, fluid/air flows, acoustic waves, and body/organ motions.[16–25]

Early efforts exploited the capability of detecting the frequency and magnitude of stimuli to further evaluate the dynamic sensing performance of piezoelectric sensors.[26–29] Some studies have been conducted to demonstrate the influence of loading frequency on the piezoelectric voltage.[30–35] A high frequency of stimuli is beneficial to the enhanced voltage, indicating that various loading rates of the stimuli can lead to the discrepancy of the piezoelectric voltage. Additional efforts on several advances on the piezoelectric sensor to perceive the magnitude of mechanical stimuli have been made.[36–38] The piezoelectric voltage increases with the applied pressure at the same frequency, which is attributed to the larger strain.

Since the frequency and magnitude of stimuli have an effect on the piezoelectric voltage simultaneously, explorations of accurately detecting the magnitude of stimuli have been carried out. Current studies have reported that the frequency response of the output piezoelectric voltage depends on the inner resistance of the voltmeter used.[39,40] They further designed an ideal voltmeter with a large inner resistance (10^{12} Ω) for measuring the magnitude of pressure. By utilizing the large inner resistance of the voltmeter in the testing circuit, the influence of the loading frequency can be eliminated to acquire the open-circuit voltage. However, the inner resistance of the commercial voltmeter is between tens of megaohms and

[a] College of Mechanical Engineering, Zhejiang University of Technology, Hangzhou 310023, China. E-mail: tianye@zjut.edu.cn, wuhuaping@gmail.com
[b] Key Laboratory of Special Purpose Equipment and Advanced Processing Technology, Ministry of Education and Zhejiang Province, Zhejiang University of Technology, Hangzhou 310023, China
[c] Center for Optoelectronics Materials and Devices, Zhejiang Sci-Tech University, Hangzhou 310018, China. E-mail: liuaiping1979@gmail.com
[d] Department of Engineering Mechanics, School of Aeronautics and Astronautics, Zhejiang University, 310027 Hangzhou, China
[e] Zhijiang College of Zhejiang University of Technology, Shaoxing 312030, China
† Electronic supplementary information (ESI) available. See DOI: 10.1039/d0tc02949a

hundreds of megaohms, which cannot completely eliminate the influence of frequency on the piezoelectric voltage. Meanwhile, although the interference of frequency to voltage is eliminated, it still limits the piezoelectric sensor in the detection of frequency-related information, such as water flow velocity and human motion velocity.[41–43] Thus, it is highly desirable to utilize the frequency response characteristics of piezoelectric voltage to detect the magnitude and loading rate of stimuli in the voltmeter test circuit with a limited inner resistance.

Herein, we elucidate the frequency-response behaviour of piezoelectric voltage of a piezoelectric sensor based on a piezoelectric enhanced composite film of P(VDF-TrFE) and $BaTiO_3$. Through quantitative matching of theoretical calculations and experimental studies, we reveal that the piezoelectric voltage enhances with an increase of frequency and becomes stable beyond the critical stable frequency. Furthermore, the critical stable frequency decreases with the enhancement of inner resistance. Such a demonstrated frequency-response behaviour of the piezoelectric sensor is illustrated by whether the loading can be completed within the period of piezoelectric voltage measurement in the testing circuit, which is further verified through systematical compression and bending measurements. Meanwhile, the flexible piezoelectric sensor successfully achieves the accurate detection of the magnitude and loading rate of stimuli by utilizing the frequency-response behaviour of the piezoelectric voltage. The practical applicability of the flexible piezoelectric sensor in the bionic flying robot is presented to monitor the flight situations (Fig. 1), thus demonstrating the potential to develop intelligent self-perception robots.

2. Experimental

2.1 Preparation of $BaTiO_3$/P(VDF-TrFE) composite film

P(VDF-TrFE) and $BaTiO_3$ composite films were prepared by using P(VDF-TrFE) powder with a molar ratio of 70/30 (Piezotech) and $BaTiO_3$ nanoparticles with an average diameter of 100 nm (Sigma-Aldrich) based on our previous work.[44] The $BaTiO_3$ nanoparticles were first mixed with *N*,*N*-dimethylformamide (DMF) and ultrasonically stirred for 2 h to separate the aggregated nanoparticles. P(VDF-TrFE) powders were then added to produce solutions with a predefined 0–20 wt% of $BaTiO_3$ nanoparticles with respect to P(VDF-TrFE) by stirring for 2 h using a magnetic stirrer at room temperature to obtain a uniform solution. Composite films of $BaTiO_3$/P(VDF-TrFE) were prepared by casting the uniform solution on a Petri dish, followed by annealing at 120 °C for 2 h to enhance crystallinity. Then, the film was placed in a silicone oil bath for half an hour at a high electric field of 60 MV m^{-1} to be polarized to obtain enhanced piezoelectric properties.

2.2 Fabrication of the piezoelectric sensors

The PDMS substrate film was prepared by spin-coating a 10 : 1 mixture of PDMS part A and part B (Sylgard 184, Dow Corning) using an EZ4 spin coater (Schwan technology). The mixture was poured onto a disc glass substrate (diameter: 9 cm). Then spin coating (1500 rpm for 30 s) was performed, followed by curing at 80 °C for 30 min. The gold electrode (thickness: 150 nm) was evaporated by an electron beam (DZS-500) on both sides of the composite film. After the copper wires were attached to the upper and lower gold electrodes, another PDMS covering layer was coated on the top and cured at 80 °C for 30 min.

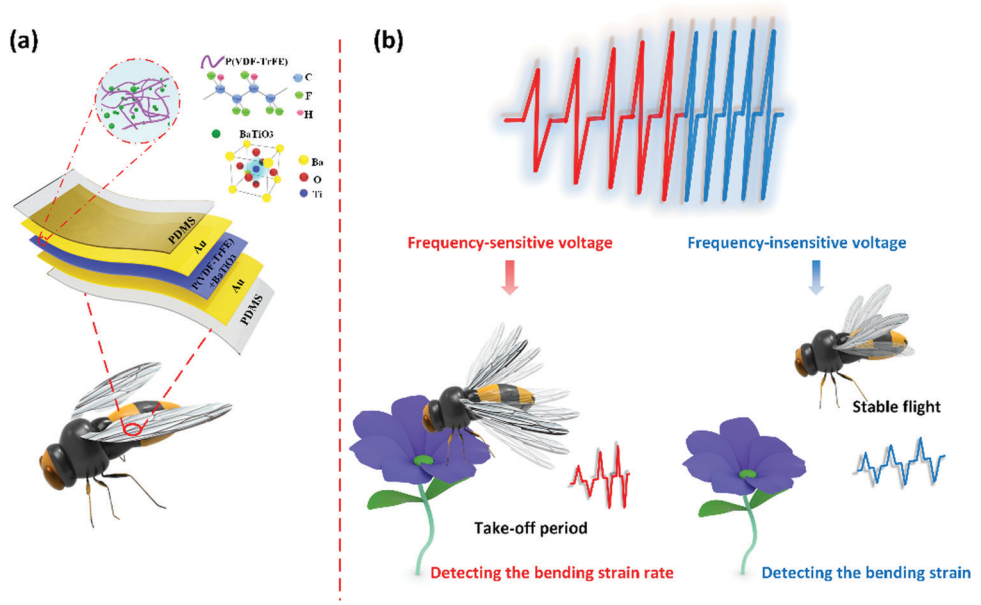

Fig. 1 Illustration of the concept of the flexible piezoelectric sensor applied to bionic flying robots. (a) Schematic configuration of the piezoelectric sensor based on a piezoelectric enhanced composite film of P(VDF-TrFE) and $BaTiO_3$, with key components, labeled. (b) The piezoelectric voltage enhances with the increase of frequency and becomes stable beyond the critical frequency. By utilizing the frequency-response behaviour in different frequency ranges, the flexible piezoelectric device is integrated with a bionic bee to monitor flight status (*i.e.*, strain rate and strain) of the vibrating wings.

The sample was cut into strips (20 mm × 20 mm × 30 μm) and carefully peeled off from the glass to obtain sandwich-structured sensors.

2.3 Characterization

The d_{33} values of the piezoelectric films were measured using a quasi-static d_{33} tester (ZJ-6A of the Chinese Academy of Sciences) at room temperature. The film was inserted into the middle of the upper and lower probes, and the handwheel was adjusted to hold the film and acquire the d_{33} value. In the case of low-frequency mechanical loading, the compression and bending tests were carried out using a mechanical testing system (Instron LEGEND2345). In the case of high-frequency loading, the sensor was positioned under a cylindrical probe (KSI-758STNG3.25), which was driven by an exciter (KSI-758MS20). The exciting signal from a high precision network data analyzer (KSI-8904N) was amplified by using a power amplifier (KSI-758PA100) to drive the vibrator. The magnitude of the force input to the sensor was measured by using a calibrated piezoelectric force transducer (KSI-208) having a sensitivity of 4 pC N^{-1}. The output from the force transducer was passed through a charge amplifier (KSI-608A100) before being recorded using a high precision network data analyser (Fig. S1, ESI†).

3. Results and discussion

In order to explore the piezoelectric characteristics of the sensor, it should be noted that the copolymers of polyvinylidene fluoride (P(VDF-TrFE)) films after poling are transversely isotropic with the polarization direction normal to the surface. Constitutive models can be used that relate the stress σ_{ij}, strain ε_{ij}, electrical field E_i, and electrical displacement D_{ij}, where c_{ij}, e_{ij}, and k_{ij} are the elastic, piezoelectric, and dielectric constants, respectively.[45,46] Consider that a uniaxial compressive stress σ_{33} ($\sigma_{11} = \sigma_{22} = 0$) is applied along the x_3 direction on a flat piezoelectric film, in which the strain ε_{ij} and the electrical field E_3 along the polarization direction satisfy the constitutive relationships: $0 = c_{11}\varepsilon_{11} + c_{12}\varepsilon_{22} + c_{13}\varepsilon_{33} - e_{31}E_3$; $0 = c_{12}\varepsilon_{11} + c_{11}\varepsilon_{22} + c_{13}\varepsilon_{33} - e_{31}E_3$; $\sigma_{33} = c_{13}\varepsilon_{11} + c_{13}\varepsilon_{22} + c_{33}\varepsilon_{33} - e_{33}E_3$; $D_3 = e_{31}\varepsilon_{11} + e_{31}\varepsilon_{22} + e_{33}\varepsilon_{33} + k_{33}E_3$. The elimination of ε_{11}, ε_{22}, and ε_{33} gives $D_3 = \bar{e}\sigma_{33}/\bar{E} + \bar{k}E_3$, where $\bar{e} = e_{33} - [2c_{13}/(c_{11} + c_{12})]e_{31}$ and $\bar{E} = c_{33} - 2{c_{13}}^2/(c_{11} + c_{12})$. Meanwhile, $\bar{k}$ can be expressed as $\bar{k} = k_{33} + [2c_{33}{e_{31}}^2 - 4c_{13}e_{31}e_{33} + (c_{11} + c_{12}){e_{33}}^2]/(c_{11}c_{33} + c_{12}c_{33} - 2{c_{13}}^2)$. The current $I = -AdD_3/\mathrm{d}t$ is related to the voltage V and resistance R of the voltmeter by $I = V/R$, which gives $V/R = -AdD_3/\mathrm{d}t$. Thus, the specific coupling of the deformation and the piezoelectric effect can be described as the following governing equation[45,46]

$$\frac{\mathrm{d}V}{\mathrm{d}t} + \frac{l}{AR\bar{k}}V = \frac{-l\bar{e}}{\bar{k}\bar{E}}\frac{\mathrm{d}\sigma_{33}}{\mathrm{d}t} \quad (1)$$

where V is the measured voltage between the two electrodes of the piezoelectric sensor, R is the inner resistance of the voltmeter, l and A are the total thickness and area of the piezoelectric film, respectively, and $\bar{e}$ and $\bar{k}$ are the effective piezoelectric constants. The material parameters used in the calculation are as follows: $c_{11} = 1.6 \times 10^9$ N m^{-2}; $c_{12} = 0.8 \times 10^9$ N m^{-2}; $c_{13} = 1.42 \times 10^9$ N m^{-2}; $c_{33} = 1.63 \times 10^9$ N m^{-2}; $e_{31} = 0.032$ C m^{-2}; $e_{33} = -0.06$ C m^{-2}.[47] Moreover, using the initial condition $V(t = 0) = 0$, the voltage is obtained as

$$V = \frac{(-\bar{e})l}{\bar{k}}\frac{F}{A\bar{E}} - \frac{(-\bar{e})l^2}{AR(\bar{k})^2}\mathrm{e}^{\frac{lt}{AR\bar{k}}}\int_0^t \frac{F}{A(\bar{E})}\mathrm{e}^{\frac{lt}{AR\bar{k}}}\mathrm{d}t \quad (2)$$

Note that the compressive stress is an approximate periodic function of time in the experiment, given by

$$F = F_{\max}[1 - \cos(2\pi ft)]/2 \quad (3)$$

where $F_{\max}$ is the maximum compressive force.

Mathematical software was used for the theoretical calculations related to the frequency-response behaviour of the piezoelectric sensor. The effects of loading frequency on the piezoelectric voltage for the voltmeters with various inner resistances are presented in Fig. 2. The voltmeter with an inner resistance of 1 MΩ is first taken into account to calculate, and the corresponding peak value of the piezoelectric voltage under a pressure of 1 kPa is obtained by eqn (2). By gradually increasing the frequency, the output voltage increases and then tends to be stable (Fig. 2a). The frequency sensing performance is evaluated by depicting the tangent of the curve on the frequency-response piezoelectric voltage change rate and calculating the slope of the tangent. The slope of the voltage curve is given by $S = \delta V/\delta f$, which represents the sensitivity to frequency. Two linear regions of voltage change rate as a function of applied frequency are observed. In the frequency regime of less than 1000 Hz, the sensitivity of the device reaches 0.47 mV Hz^{-1}. When the applied frequency is higher than 1000 Hz, the sensitivity of the device is 0.17 mV Hz^{-1}. The sensitivity is reduced to approximately zero, indicating that the piezoelectric voltage tends to be saturated. The quantitative definition of the critical stable frequency has been proposed to clarify the frequency-response behaviour. At first, two linear regions of voltage variation as a function of applied frequency require good linearity and sensitivity. High linearity (*i.e.*, $R^2 > 95\%$) is also a critical performance of the sensor,[48,49] and two linear regions are fitted separately to maintain the linearity of each segment above 95%. Besides, the relative change between the voltage and the saturated voltage begins to be less than 5%, and the frequency corresponding to the voltage can be defined as the critical stable frequency. The relative change of 5% between the stable voltage and the selected saturation voltage is based on the stability determination in the previous literature[50–52] and the judgment of the stability of the step response with a similar change trend in the control system. The specific critical stable frequency of the voltmeter with 1 MΩ inner resistance is *ca.* 1855 Hz. The inset in Fig. 2a shows the real-time change curves of voltage with time under different frequencies, and the corresponding peak value is marked to verify the frequency-response behaviour.

The same trend of voltage change also appears in the voltmeter with 10 MΩ and 1 TΩ inner resistances (Fig. 2b and c). Moreover, the critical stable frequencies *via* different voltmeters are significantly different, indicating that the

frequency-response behaviour of the output voltage depends on the inner resistance. To further clarify this influence, the inner resistances in the range of 1 MΩ to 1 TΩ are calculated to obtain the corresponding critical stable frequency. The critical stable frequency decreases with the increase of the inner resistance (Fig. 2d), which demonstrates that the dependence on frequency can be very large for the small-resistance voltmeter. This conclusion illustrates that a reasonable selection of inner resistance of voltmeter has practical significance. For instance, the frequency independence of the voltmeter with a large inner resistance can be used to detect the magnitude of the pressure. The requirement of detecting the loading rate of pressure is more inclined to choose a voltmeter with a small inner resistance.

This frequency-response behaviour can be well explained by a piezoelectric physical model shown in Fig. 3. The mechanism of piezoelectric voltage generation is described in the schematic illustration. The mechanical pressure reorients the aligned molecular dipoles, causing an internal piezoelectric potential.[43–56] The free charge carriers presented at the metal electrodes flow from the higher potential region to the lower potential region through the external connections to balance the internal piezoelectric potential, thus giving rise to a positive peak. When the pressure is released, the change in the polarization diminishes, and hence the internal piezoelectric potential falls to zero, such that the free-charge carriers return across the external circuit, giving rise to a negative peak.[57–60] Thus, the waveform of the piezoelectric voltage is an instantaneous pulse wave, thereby leading the voltage to have a short measurement time required by the generation and decay of the piezoelectric charge (enlarged view). Meanwhile, more charges accumulated during this measurement time will lead to a higher output voltage. For a voltmeter with a finite inner resistance in the measuring circuit, the electrical charge on electrodes of the piezoelectric layer can go through the voltmeter during measurement, instead of an ideal open circuit.[40] The output voltage obtained by the smaller inner resistance voltmeter increases and decays rapidly, illustrating that the charge can go through the voltmeter freely during the cyclical movement. In contrast, the decay time of the output voltage tested by the larger inner resistance voltmeter is much larger than the case of smaller resistance, and the status of the circuit approaches that of the ideal open circuit during the voltage measurement. Thus, the longer measurement time induced by a larger inner resistance of the voltmeter enables more time to load, which shows the small frequency dependence of the

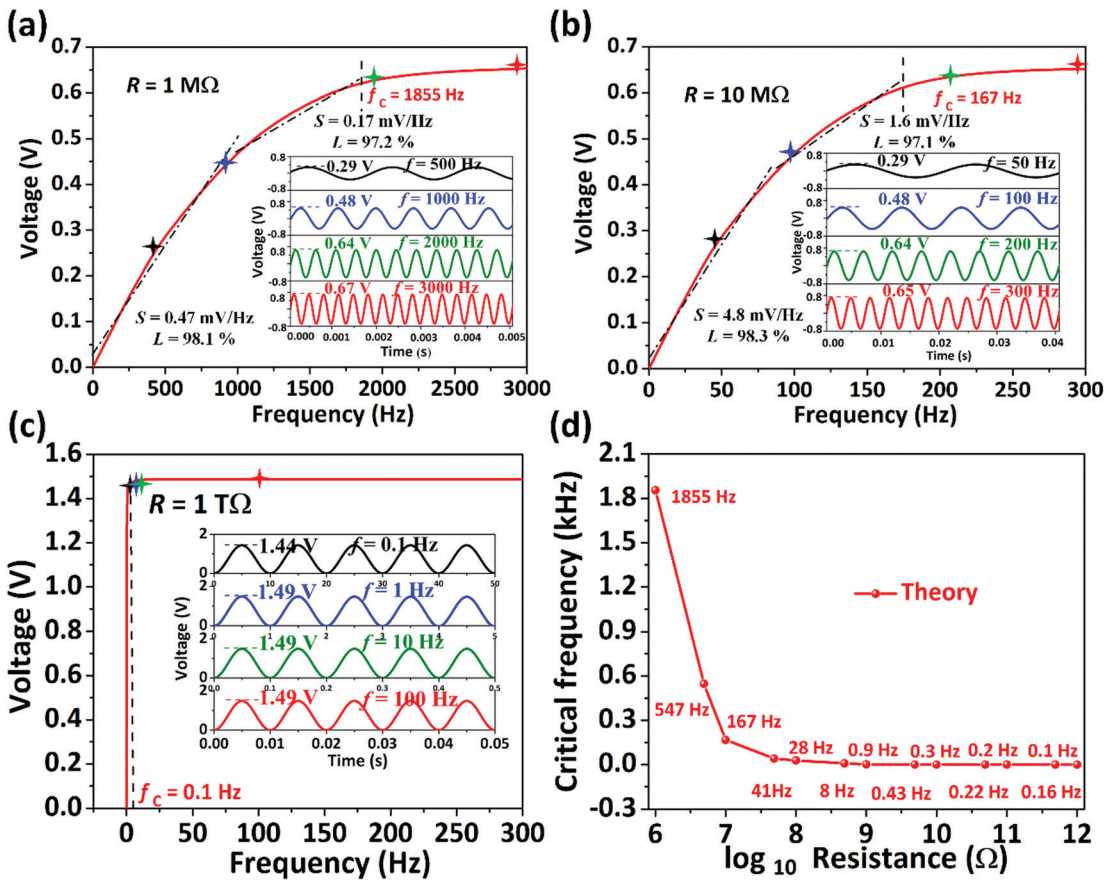

Fig. 2 Theoretical studies on the output voltage of the piezoelectric sensor under different frequencies with a pressure at 1 kPa. Effects of loading frequency on the output piezoelectric voltage for the voltmeters with resistances of (a) 1 MΩ, (b) 10 MΩ, and (c) 1 TΩ. (d) The critical stable frequency *versus* the inner resistance of voltmeter in the range from 1 MΩ to 1 TΩ.

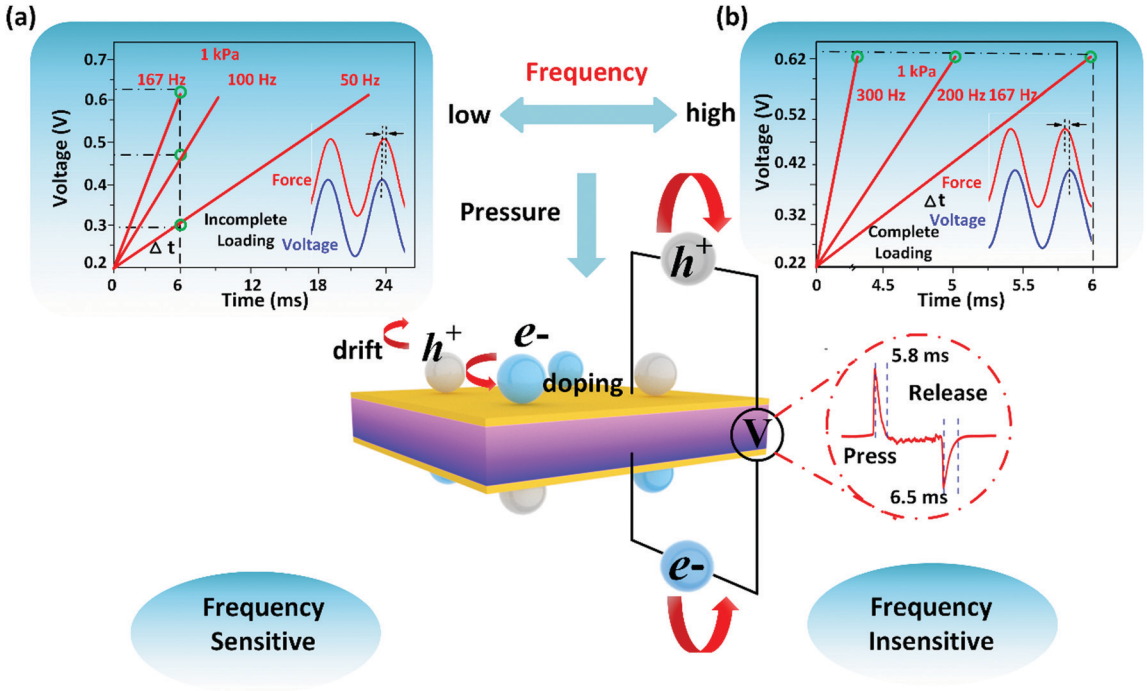

Fig. 3 Schematic illustrations of the frequency-response behaviour of piezoelectric voltage based on the piezoelectric mechanism. (a) The peak values of the piezoelectric voltage obtained by the 10 MΩ voltmeters at an applied pressure of 1 kPa with the loading frequencies of 50, 100, and 167 Hz show the frequency-sensitive behaviour. The curves in the inset show the phase shift between the piezoelectric voltage and loading force with a loading frequency of 100 Hz. (b) The peak values of piezoelectric voltage obtained by the 10 MΩ voltmeters at an applied pressure of 1 kPa with the loading frequencies of 167, 200, and 300 Hz demonstrate the frequency-insensitive behaviour. The curves in the inset show the phase shift between the voltage and force with a loading frequency of 200 Hz.

output voltage. It can also effectively prove that the frequency-dependent response of the output voltage depends on the inner resistance, and the critical stable frequency decreases with the increase of the inner resistance.

Furthermore, several theoretical examples are used to illustrate the response of voltage to frequency (Fig. 3). The values marked by the green circles are the calculated piezoelectric voltages at different frequencies with a loading pressure of 1 kPa during the measurement time. For instance, the specific critical stable frequency of the voltmeter with a 10 MΩ inner resistance is *ca.* 167 Hz as shown in Fig. 2b, which shows that this pressure can be fully loaded with a measurement time of 6 ms. The corresponding piezoelectric voltages of 50, 100, and 167 Hz pressure are 0.29, 0.48, and 0.64 V, illustrating the frequency dependence of the voltage (Fig. 3a). The loading time induced by the small frequency is larger than the measurement time, which leads to an incomplete collection of the piezoelectric charge. The incomplete loading can also be quantitatively verified from the voltage and pressure curves. Although the loading pressure continues, the free-charge carriers have already returned across the external circuit, giving rise to a negative peak. Therefore, the peak value of the voltage is before the peak value of the force (the inset curve in Fig. 3a and Fig. S4a, ESI† measured by the experimental setup of Fig. S1, ESI†). This means that the maximum pressure effectively sensed by the sensor during the measurement time is less than the loading pressure of 1 kPa, resulting in a decrease of the output voltage. In contrast, the voltage output at an applied pressure of 1 kPa with loading frequencies of 200 and 300 Hz is approximately equal to that with the 167 Hz loading, which is attributed to the same charge accumulation. In the high-frequency loading, the periods of voltage measurement are larger than the loading time, leading to a complete loading of the pressure. Meanwhile, the voltage peak value is after the pressure peak value (the inset curve in Fig. 3b and Fig. S4b, ESI†) due to the phase shift between the input pressure signal and the output voltage. This also can clarify that the peak value of the voltage sensed by the sensor corresponds to the loading maximum pressure of 1 kPa. In conclusion, these frequency response features depend on whether the stimuli can be completely loaded at a period of voltage measurement. Therefore, the output voltage of the piezoelectric sensor exhibits frequency-sensitive behaviour below the critical frequency of stimuli and exhibits frequency-insensitive behaviour above the critical frequency of stimuli.

Experimental demonstrations are then conducted to further verify the frequency response behaviour of piezoelectric voltage. Piezoelectric polymers P(VDF-TrFE) with high flexibility are potential candidates for flexible sensors, but their low d_{33} should be improved for high-performance e-skins. In contrast, inorganic piezoelectric materials (*e.g.*, $BaTiO_3$ and lead zirconium titanate PZT)[61] exhibit high piezoelectric coefficients, but their intrinsic rigidity restricts their application in flexible electronics. Thus, incorporating inorganic piezoelectric fillers

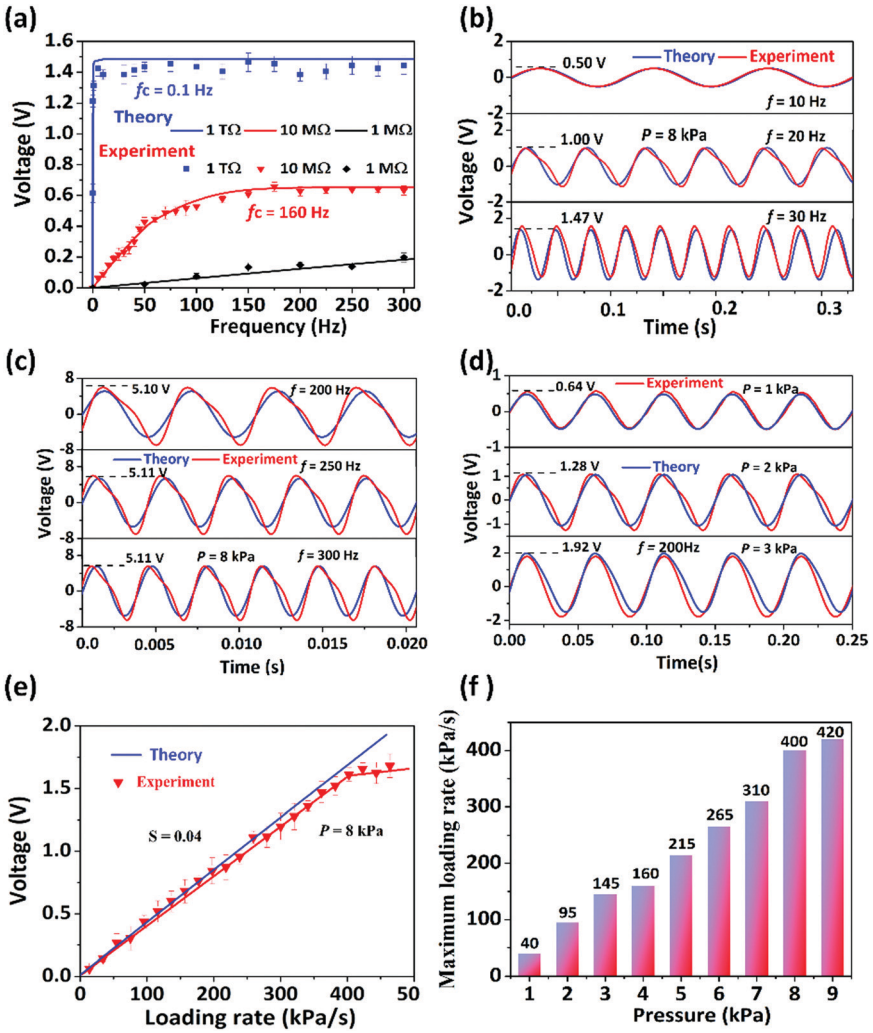

Fig. 4 Experimental and theoretical studies on the output voltage of the piezoelectric sensor under different loading frequencies. (a) Comparison between theory and experiments values of voltage *versus* the loading frequency obtained by the voltmeters with resistances of 1 TΩ, 10 MΩ, and 1 MΩ under a pressure of 1 kPa. Effects of loading frequency on the output voltage obtained by the 10 MΩ voltmeter at an applied pressure of 8 kPa with the loading frequency of (b) 10, 20, and 30 Hz; (c) 200, 250, and 300 Hz. (d) Effects of pressure magnitude on the output voltage obtained by the 10 MΩ voltmeter at the same loading frequency of 200 Hz. (e) The comparison between theoretical predictions and experimental measurements of voltage *versus* the loading rate obtained by the voltmeters with a resistance of 10 MΩ under the pressure of 8 kPa. (f) Maximum detectable loading rate under different magnitudes of pressure in experiments.

such as $BaTiO_3$ into the piezoelectric polymer matrices represents a simple method to improve their piezoelectric properties, owing to the simplicity and cost-effectiveness of this method.[62–65] In this work, the flexible piezoelectric sensor was composed of five layers, including the piezoelectric film, two Au electrodes, and two spin-coated PDMS layers (Fig. 1a). The enlarged view of the piezoelectric film indicates that the sensing layer is based on $BaTiO_3$ nanoparticles embedded into highly crystalline P(VDF-TrFE) polymers. Comprehensive phase characterization of P(VDF-TrFE) films and $BaTiO_3$ nanoparticles was confirmed by X-ray diffraction (XRD) and Fourier transform infrared spectroscopy (FTIR) analyses as shown in Fig. S2a and b (ESI†). Nanocomposite films with a predefined 0–20 wt% of $BaTiO_3$ nanoparticles with respect to P(VDF-TrFE) were prepared and tested to find an optimized doping ratio. The magnified scanning electron microscopy (SEM) images show the uniform distribution of composites, which reveals excellent interfacial adhesion between $BaTiO_3$ particles and the P(VDF-TrFE) matrix (Fig. S3, ESI†). The ability of piezoelectric materials to convert vertical mechanical deformation into an electric signal can be represented by the piezoelectric coupling coefficient. The d_{33} values of pure P(VDF-TrFE) films and P(VDF-TrFE) films with 10 wt% $BaTiO_3$ nanoparticles are 19 and 35.9 pC N^{-1} (Fig. S2c, ESI†), respectively. The corresponding piezoelectric coefficient e_{33} of the composite film is obtained to be 0.058 C m^{-2}, which is in good agreement with the theoretical calculation. The enhanced piezoelectricity of the P(VDF-TrFE)/$BaTiO_3$ composites is mainly attributed to the combination of piezoelectric crystalline-phase with the high piezoelectric coefficient of $BaTiO_3$ fillers.[66] Besides, previous research indicates that $BaTiO_3$ nanoparticles can reinforce the local stress of the P(VDF-TrFE) matrix and induce large local

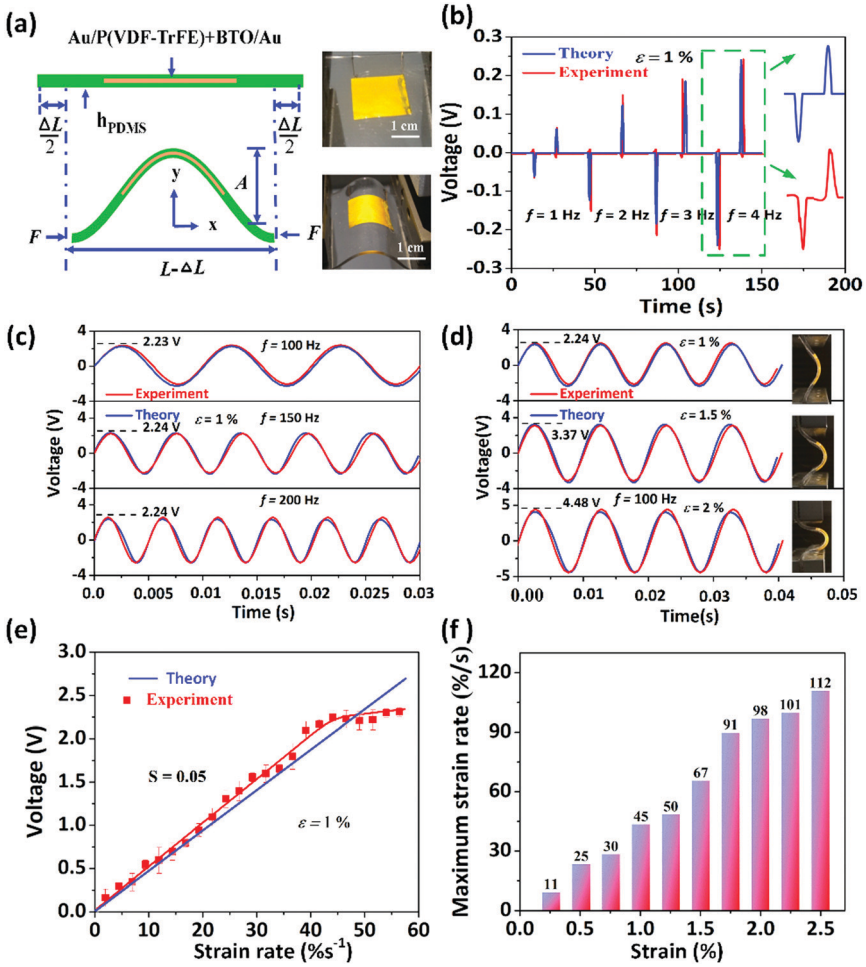

Fig. 5 Experimental and theoretical studies on the output voltage of the piezoelectric sensor under different bending frequencies. (a) Schematic illustration of an analytical model for the coupling of mechanical deformation with piezoelectric response during bending. Photographs of the piezoelectric sensor clamped on a bending stage in flat and bend configurations. Effects of bending frequency on the output voltage for the frequency of (b) 1, 2, 3, and 4 Hz; (c) 100, 150, and 200 Hz. (d) Effects of strain on the output voltage at the same bending frequency of 100 Hz. (e) The comparison between theoretical predictions and experimental measurements of voltage *versus* the strain rate obtained by the voltmeters with the resistance of 10 MΩ under a strain of 1%. (f) Maximum detectable strain rate under the different strains of bending in experiments.

deformation of the composites, leading to an improvement of piezoelectric properties.[67]

For evaluating the sensing performance of piezoelectric sensors in the experiment, three voltmeters with inner resistances of 1 TΩ, 10 MΩ, and 1 MΩ are used for the voltage measurement. The good agreement between the analytical prediction obtained from eqn (2) and the experimental result further validates the frequency-response behaviour of the output voltage (Fig. 4a). The voltage measured using the 1 TΩ large inner resistance voltmeter is weakly dependent on frequency, and the small linear range of voltage leads to a critical stable frequency of 0.1 Hz. In contrast, the voltage obtained using the 1 MΩ resistance voltmeter increases linearly with frequency in the range of 0 to 300 Hz. Meanwhile, the voltage acquired using the 10 MΩ resistance voltmeter presents a stable trend when the frequency is above 160 Hz, thereby indicating that the piezoelectric sensor exhibits a wide range of frequency-sensitive and frequency-insensitive behaviours. To investigate the influence of the frequency on the voltage more comprehensively, experimental demonstrations are then conducted based on the voltmeter with a 10 MΩ inner resistance. The measured output voltage curves at a pressure of 8 kPa with 10, 20, and 30 Hz show that the peak value depends on the frequency of loading (Fig. 4b). The frequency-sensitive behaviour is consistent with the effect of loading frequency on piezoelectric voltage in literature studies.[30–35] With a further increase in the frequency, the output voltages for frequencies of 200, 250, and 300 Hz remain stable (Fig. 4c), which confirms the frequency-insensitive behaviour of the output voltage. It is also observed in some research that the peak value of the output voltage has no obvious change with various force/bending frequencies,[50,51,68,69] which is regarded as the stability advantage of the sensor.

This newly discovered finding of the frequency-response behaviour makes piezoelectric sensors have more extensive application potential in accurately detecting the magnitude and loading rate of pressure. As a proof-of-concept demonstration, the piezoelectric sensor is exploited to acquire the capability of detecting the magnitude of pressure. In the measurement

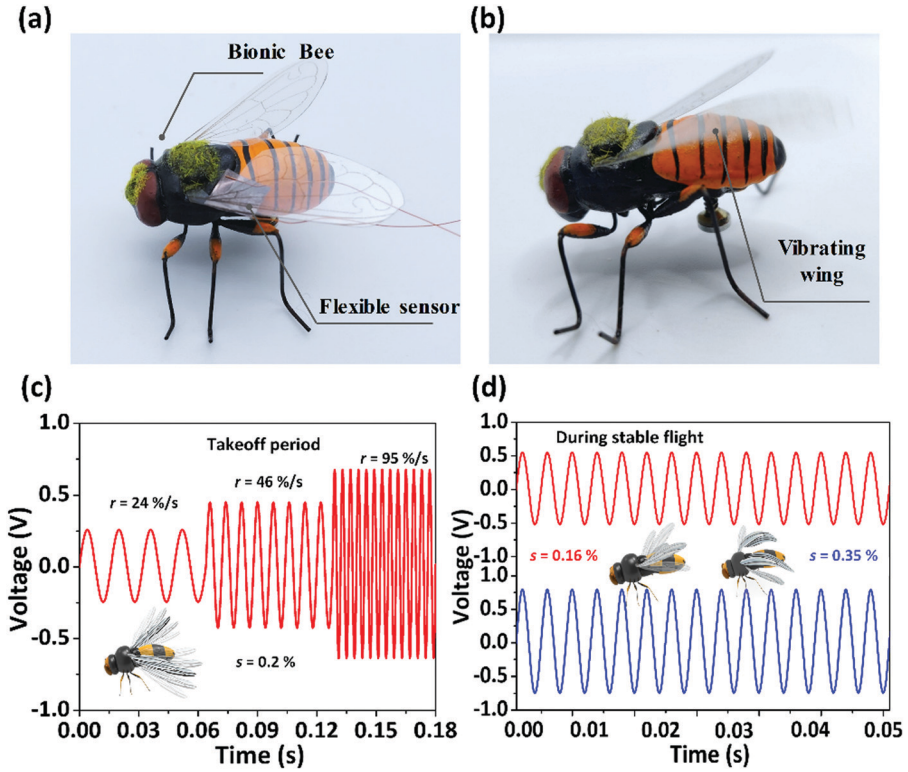

Fig. 6 Practical application of flexible piezoelectric sensors for bionic flying robots. (a) A photograph of the flexible piezoelectric sensor attached to the wing of a bionic bee. (b) A photograph of the vibrating wing of the bionic bee. (c) The voltage detected by the piezoelectric sensor shows the strain rate (r = 24% s^{-1}, 46% s^{-1}, and 95% s^{-1}) of the vibrating wing in the take-off period. (d) The voltage detected by the piezoelectric sensor shows the strain (s = 0.16%, 0.35%) of the vibrating wing in the high-frequency flight period.

circuit of the voltmeter with 10 MΩ inner resistance, loading frequencies above the critical frequency (160 Hz) can be applied to accurately detect the magnitude of the pressure, which is attributed to the frequency-insensitive behaviour of the piezoelectric voltage. The piezoelectric voltages under the pressures of 1, 2, and 3 kPa at 200 Hz are recorded (Fig. 4d). Larger pressure yields larger compressive strain, and therefore, higher voltage values can be seen. Meanwhile, the voltage below the critical frequency is affected by the frequency and the magnitude of the pressure, but the change of the voltage is essentially caused by the loading rate. The simultaneous change of loading time and strain induces a change of strain rate sensed by the piezoelectric sensor. Thus, the loading frequency below the critical frequency can be utilized to detect the loading rate. To further evaluate the potential of detecting the loading rate of pressure, the output voltage *versus* the loading rate is displayed in Fig. 4e. The detailed derivation process is included in the ESI† (S5). The theoretical predictions of voltage *versus* the loading rate are consistent with the experimental measurements. The only difference is that the theoretical loading rate is proportional to the magnitude of pressure, and the larger voltage induced by the larger pressure causes the curve to be unsaturated. In contrast, upon increasing the magnitude of the pressure in experiments, the centers of both positive and negative charge carrier separations reach a maximum value (*i.e.*, the maximum number of dipoles will orient in one direction), resulting in a saturated piezoelectric voltage.[41] Meanwhile, the maximum detection of loading rate corresponding to the pressure ranging from 1 kPa to 9 kPa is determined through the compression tests (Fig. 4f), providing guidance for the practical application of detecting the loading rate.

The sensing capability of the flexible piezoelectric sensors on bending deformation also needs to be explored. An analytical model for the coupling mechanical deformation and piezoelectric response during bending of the piezoelectric sensor is shown in Fig. 5a. The specific coupling of the bending deformation and the piezoelectric effect of the sensor can be described as the following governing equation

$$V = \frac{(-\bar{e})l}{\bar{k}}\frac{\varepsilon}{A\bar{E}} - \frac{(-\bar{e})l^2}{AR(\bar{k})^2}e^{\frac{lt}{AR\bar{k}}}\int_0^t \frac{\varepsilon}{A(\bar{E})}e^{\frac{lt}{AR\bar{k}}}dt \qquad (4)$$

Where $\varepsilon = \varepsilon_{max}[1 - \cos(2\pi ft)]/2$, V is the measured voltage between the two electrodes of the piezoelectric sensor, R is the inner resistance of voltmeter, l and A are the total thickness and area of the piezoelectric film, respectively, and $\bar{e} = e_{31} - (c_{13} - c_{33})e_{33}$ and $\bar{k} = k_{33} + (e_{33}^2/c_{33})$ are the effective piezoelectric constants.

To further prove the effect of bending frequency on piezoelectric output, the piezoelectric sensor clamped on a bending stage in flat and bend configurations is measured for the output voltage (Fig. 5a). The piezoelectric sensor is experimentally subjected to cycling bending tests at various frequencies.

The output voltage increases (Fig. 5b) and tends to be stable (Fig. 5c) with the increasing frequency under the same strain (ε = 1%). The finding in bending tests is similar to the loading of pressure, which presents the frequency-response behaviour in different frequency ranges. This frequency-response characteristic enables the piezoelectric sensor to be used to detect the bending strain ad strain rate. The distinguishment of strain at 1%, 1.5%, and 2% can further prove the sensing capability in detecting the strain (Fig. 5d). Meanwhile, the voltage increases with the increase of the strain rate for a given strain (ε = 1%), illustrating the great potential in detecting the strain rate (Fig. 5e). The maximum detectable strain rate under different strains ranging from 0.25% to 2.5% is demonstrated to provide insights into the practical application (Fig. 5f).

Effectively detecting the bending strain and strain rates creates application opportunities for the piezoelectric sensors in bionic flying robots. The bionic flying robot named robobee has been successfully developed with a bumblebee (flapping frequency 180–250 Hz) as the bionic object in nature, which is of great significance to the field of micro flapping robots.[70–76] It is essential for the self-sensing function of the bionic flying robot to monitor the deformation of its wings in real-time. A flexible piezoelectric sensor (dimension: 5 mm × 5 mm) is attached to the wing of the bionic bee (Fig. 6a). The strain rate and strain of the vibrating wing shown in Fig. 6b can be detected by using the frequency response characteristics of piezoelectric voltages in different frequency ranges. In the low-frequency takeoff period of the bionic robot, the voltage is simultaneously affected by the frequency and strain of the bending, which induces a change of strain rate sensed by the piezoelectric sensor. Thus, the voltage detected by the piezoelectric sensor (Fig. S6, ESI†) shows that the strain rates of the wing are 24% s^{-1}, 46% s^{-1}, and 95% s^{-1} as observed from Fig. 6c. In contrast, the frequency-insensitive behaviour of the piezoelectric voltage during the stable flight can be applied to accurately detect the strain of the bending wing. The voltages generated by the piezoelectric sensor declare that the stable strains of the vibrating wing of the bionic robot are 0.16% and 0.35% during the high-frequency stable flight as shown in Fig. 6d. The 3D scanner (PD13D) has been used to verify the accuracy of the strain rate and strain, and the average relative error is controlled within 10% (Fig. S7, ESI†). The demonstration in Fig. 6 shows the capability of the piezoelectric sensor to detect the bending strain rate and bending strain of the vibrating wing of the bionic bee. This flexible piezoelectric sensor enables the bionic flying robot to precisely monitor its flight situation in real-time, thus making the bionic robot more autonomous and intelligent.

4. Conclusion

In summary, we have demonstrated a frequency-response behaviour of flexible piezoelectric sensors made of highly crystalline P(VDF-TrFE) polymers with $BaTiO_3$ nanoparticles embedded. Through a comprehensive set of theoretical calculations and experimental tests, it is observed that the piezoelectric voltage increases with the applied frequency and then remains stable once the critical frequency is exceeded. The critical stable frequency decreases with the increase of inner resistance. This unique feature is determined by whether the loading can be completed within the period of piezoelectric measurement in the testing circuit. The compression and bending tests further reveal that the sensor can use this frequency-dependent behaviour to detect the magnitude and loading rate of stimuli. Furthermore, the flexible piezoelectric sensor is integrated with a bionic flying robot to monitor the flight situation, which promotes the applicability of piezoelectric devices in the field of intelligent robots.

Conflicts of interest

There are no conflicts to declare.

Acknowledgements

This work was supported by the National Science Foundation of China (Grant no. 11672269, 11972323, 51572242 and 51675485), the Zhejiang Provincial Natural Science Foundation of China (Grant no. LR20A020002, LR19E020004, and LR18E050002), the Fundamental Research Funds for the Provincial Universities of Zhejiang (RF-B2019004), the 111 Project (No. D16004), and the Zhejiang Lab's International Talent Fund for Young Professionals.

References

1 J. Heikenfeld, A. Jajack, J. Rogers, P. Gutruf, L. Tian, T. Pan, R. Li, M. Khine, J. Kim, J. Wang and J. Kim, *Lab Chip*, 2018, **18**, 217–248.
2 Y. Yang and W. Gao, *Chem. Soc. Rev.*, 2019, **48**, 1465–1491.
3 Y. Kim, A. Chortos, W. T. Xu, Y. X. Liu, J. Y. Oh, D. Son, J. Kang, A. M. Foudeh, C. X. Zhu, Y. Lee, S. M. Niu, J. Liu, R. Pfattner, Z. N. Bao and T. W. Lee, *Science*, 2018, **360**, 998–1003.
4 G. Chen, N. Matsuhisa, Z. Y. Liu, D. P. Qi, P. Q. Cai, Y. Jiang, C. J. Wan, Y. J. Cui, W. R. Leow, Z. J. Liu, S. X. Gong, K. Q. Zhang, Y. Cheng and X. D. Chen, *Adv. Mater.*, 2018, **30**, 1800129.
5 Q. L. Hua, J. L. Sun, H. T. Liu, R. R. Bao, R. M. Yu, J. Y. Zhai, C. F. Pan and Z. L. Wang, *Nat. Commun.*, 2018, **9**, 244.
6 D. Son, J. Kang, O. Vardoulis, Y. Kim, N. Matsuhisa, J. Y. Oh, J. W. F. To, J. W. Mun, T. Katsumata, Y. X. Liu, A. F. McGuire, M. Krason, F. Molina-Lopez, J. Ham, U. Kraft, Y. Lee, Y. Yun, J. B. H. Tok and Z. N. Bao, *Nat. Nanotechnol.*, 2018, **13**, 1057–1065.
7 C. J. Wang, K. Sim, J. Chen, H. Kim, Z. Y. Rao, Y. H. Li, W. Q. Chen, J. Z. Song, R. Verduzco and C. J. Yu, *Adv. Mater.*, 2018, **30**, 1706695.
8 J. Zhu, J. J. Fox, N. Yi and H. Y. Cheng, *ACS Appl. Mater. Interfaces*, 2019, **11**, 8867–8877.

9 L. H. Li, H. Y. Xiang, Y. Xiong, H. Zhao, Y. Y. Bai, S. Q. Wang, F. Q. Sun, M. M. Hao, L. Liu, T. Li, Z. H. Peng, J. Q. Xu and T. Zhang, *Adv. Sci.*, 2018, **5**, 1800558.
10 W. Z. Xu, Y. Xing, J. Liu, H. P. Wu, Y. Cuo, D. W. Li, D. Y. Guo, C. R. Li, A. P. Liu and H. Bai, *ACS Nano*, 2019, **13**, 7930–7938.
11 Z. N. Zou, C. P. Zhu, Y. Li, X. F. Lei, W. Zhang and J. L. Xiao, *Sci. Adv.*, 2018, **4**, eaaq0508.
12 Y. Gao, Q. Li, R. Y. Wu, J. Sha, Y. F. Lu and F. Z. Xuan, *Adv. Funct. Mater.*, 2019, **29**, 1806786.
13 K. Sim, Z. L. Rao, Z. N. Zou, F. Ershad, J. M. Lei, A. Thukral, J. Chen, Q. A. Huang, J. L. Xiao and C. J. Yu, *Sci. Adv.*, 2019, **5**, eaav9653.
14 C. J. Wan, G. Chen, Y. M. Fu, M. Wang, N. Matsuhisa, S. W. Pan, L. Pan, H. Yang, Q. Wan, L. Q. Zhu and X. D. Chen, *Adv. Mater.*, 2018, **30**, 1801291.
15 Z. S. Lv, Y. F. Luo, Y. X. Tang, J. Q. Wei, Z. Q. Zhu, X. R. Zhou, W. L. Li, Y. Zeng, W. Zhang, Y. Y. Zhang, D. P. Qi, S. W. Pan, X. J. Loh and X. D. Chen, *Adv. Mater.*, 2018, **30**, 1704531.
16 X. Ning, X. G. Yu, H. L. Wang, R. J. Sun, R. E. Corman, H. B. Li, C. M. Lee, Y. G. Xue, A. Chempakasseril, Y. Yao, Z. Q. Zhang, H. W. Luan, Z. Z. Wang, W. Xia, X. Feng, R. H. Ewoldt, Y. G. Huang, Y. H. Zhang and J. A. Rogers, *Sci. Adv.*, 2018, **4**, eaat8313.
17 Y. W. Su, S. A. Li, R. Li and C. Dagdeviren, *Appl. Phys. Lett.*, 2015, **107**, 041905.
18 C. Dagdeviren, F. Javid, P. Joe, T. von Erlach, T. Bensel, Z. J. Wei, S. Saxton, C. Cleveland, L. Booth, S. McDonnell, J. Collins, A. Hayward, R. Langer and G. Traverso, *Nat. Biomed. Eng.*, 2017, **1**, 807–817.
19 C. H. Wang, X. S. Li, H. J. Hu, L. Zhang, Z. L. Huang, M. Y. Lin, Z. R. Zhang, Z. N. Yin, B. Huang, H. Gong, S. Bhaskaran, Y. Gu, M. Makihata, Y. X. Guo, Y. S. Lei, Y. M. Chen, C. F. Wang, Y. Li, T. J. Zhang, Z. Y. Chen, A. P. Pisano, L. F. Zhang, Q. F. Zhou and S. Xu, *Nat. Biomed. Eng.*, 2018, **2**, 687–698.
20 T. Ha, J. Tran, S. Y. Liu, H. Jang, H. Jeong, R. Mitbander, H. Huh, Y. T. Qiu, J. Duong, R. L. Wang, P. L. Wang, A. Tandon, J. Sirohi and N. S. Lu, *Adv. Sci.*, 2019, **6**, 1900290.
21 H. L. Zhou, Y. Zhang, Y. Qiu, H. P. Wu, W. Y. Qin, Y. B. Liao, Q. M. Yu and H. Y. Cheng, *Biosens. Bioelectron.*, 2020, **168**, 112569.
22 X. Han, X. Chen, X. Tang, Y.-L. Chen, J.-H. Liu and Q.-D. Shen, *Adv. Funct. Mater.*, 2016, **26**, 3640.
23 G. Z. Zhang, P. Zhao, X. S. Zhang, K. Han, T. K. Zhao, Y. Zhang, C. K. Jeong, S. L. Jiang, S. L. Zhang and Q. Wang, *Energy Environ. Sci.*, 2018, **11**, 2046–2056.
24 K. Y. Chun, Y. J. Son, E. S. Jeon, S. Lee and C. S. Han, *Adv. Mater.*, 2018, **30**, 1706299.
25 Y. Lee, J. Park, S. Cho, Y. E. Shin, H. Lee, J. Kim, J. Myoung, S. Cho, S. Kang, C. Baig and H. Ko, *ACS Nano*, 2018, **12**, 4045–4054.
26 D. B. Deutz, N. T. Mascarenhas, J. B. J. Schelen, D. M. de Leeuw, S. van der Zwaag and P. Groen, *Adv. Funct. Mater.*, 2017, **27**, 1700728.
27 D. Y. Park, D. J. Joe, D. H. Kim, H. Park, J. H. Han, C. K. Jeong, H. Park, J. G. Park, B. Joung and K. J. Lee, *Adv. Mater.*, 2017, **29**, 1702308.
28 J.-H. Lee, H.-J. Yoon, T. Y. Kim, M. K. Gupta, J. H. Lee, W. Seung, H. Ryu and S.-W. Kim, *Adv. Funct. Mater.*, 2015, **25**, 3203–3209.
29 V. Bhavanasi, V. Kumar, K. Parida, J. Wang and P. S. Lee, *ACS Appl. Mater. Interfaces*, 2016, **8**, 521–529.
30 Y. Huang, Y. Ding, J. Bian, Y. Su, J. Zhou, Y. Duan and Z. Yin, *Nano Energy*, 2017, **40**, 432–439.
31 H. Gullapalli, V. S. M. Vemuru, A. Kumar, A. Botello-Mendez, R. Vajtai, M. Terrones, S. Nagarajaiah and P. M. Ajayan, *Small*, 2010, **6**, 1641–1646.
32 K. Parida, V. Bhavanasi, V. Kumar, R. Bendi and P. S. Lee, *Nano Res.*, 2017, **10**, 3557–3570.
33 W. Li, N. Wu, J. Zhong, Q. Zhong, S. Zhao, B. Wang, X. Cheng, S. Li, K. Liu, B. Hu and J. Zhou, *Adv. Funct. Mater.*, 2016, **26**, 1964–1974.
34 N. R. Alluri, S. Selvarajan, A. Chandrasekhar, B. Saravanakumar, J. H. Jeong and S.-J. Kim, *Compos. Sci. Technol.*, 2017, **142**, 65–78.
35 L. Gu, N. Y. Cui, L. Cheng, Q. Xu, S. Bai, M. M. Yuan, W. W. Wu, J. M. Liu, Y. Zhao, F. Ma, Y. Qin and Z. L. Wang, *Nano Lett.*, 2013, **13**, 91–94.
36 L. Persano, C. Dagdeviren, C. Maruccio, L. De Lorenzis and D. Pisignano, *Adv. Mater.*, 2014, **26**, 7574–7580.
37 J. Chun, N.-R. Kang, J.-Y. Kim, M.-S. Noh, C.-Y. Kang, D. Choi, S.-W. Kim, Z. L. Wang and J. M. Baik, *Nano Energy*, 2015, **11**, 1–10.
38 Z. Zhang, C. Yao, Y. Yu, Z. Hong, M. Zhi and X. Wang, *Adv. Funct. Mater.*, 2016, **26**, 6760–6765.
39 Y. Su, C. Dagdeviren and R. Li, *Adv. Funct. Mater.*, 2015, **25**, 5320–5325.
40 Y. Su, S. Li, Y. Huan, R. Li, Z. Zhang, P. Joe and C. Dagdeviren, *Extreme Mech. Lett.*, 2017, **15**, 10–16.
41 N. R. Alluri, B. Saravanakumar and S.-J. Kim, *ACS Appl. Mater. Interfaces*, 2015, **7**, 9831–9840.
42 W. Li, S. Zhao, N. Wu, J. Zhong, B. Wang, S. Lin, S. Chen, F. Yuan, H. Jiang, Y. Xiao, B. Hu and J. Zhou, *ACS Appl. Mater. Interfaces*, 2017, **9**, 23716–23722.
43 C. Lang, J. Fang, H. Shao, X. Ding and T. Lin, *Nat. Commun.*, 2016, **7**, 11108.
44 X. Zhang, Y. Wang, Y. Sheng, H. Ye, L. Xu and H. Wu, *Chem. Phys. Lett.*, 2019, **723**, 89–95.
45 L. Persano, C. Dagdeviren, Y. Su, Y. Zhang, S. Girardo, D. Pisignano, Y. Huang and J. A. Rogers, *Nat. Commun.*, 2013, **4**, 1633.
46 C. Dagdeviren, B. D. Yang, Y. Su, P. L. Tran, P. Joe, E. Anderson, J. Xia, V. Doraiswamy, B. Dehdashti, X. Feng, B. Lu, R. Poston, Z. Khalpey, R. Ghaffari, Y. Huang, M. J. Slepian and J. A. Rogers, *Proc. Natl. Acad. Sci. U. S. A.*, 2014, **111**, 1927–1932.
47 X. Chen, H. Tian, X. Li, J. Shao, Y. Ding, N. An and Y. Zhou, *Nanoscale*, 2015, **7**, 11536–11544.
48 M. Amjadi, M. Turan, C. P. Clementson and M. Sitti, *ACS Appl. Mater. Interfaces*, 2016, **8**, 5618–5626.
49 X. Q. Liao, Q. L. Liao, Z. Zhang, X. Q. Yan, Q. J. Liang, Q. Y. Wang, M. H. Li and Y. Zhang, *Adv. Funct. Mater.*, 2016, **26**, 3074–3081.

50 H. He, Y. Fu, W. Zang, Q. Wang, L. Xing, Y. Zhang and X. Xue, *Nano Energy*, 2017, **31**, 37–48.
51 C. Y. Dong, Y. M. Fu, W. L. Zang, H. X. He, L. L. Xing and X. Y. Xue, *Appl. Surf. Sci.*, 2017, **416**, 424–431.
52 M. Ha, S. Lim, J. Park, D. S. Um, Y. Lee and H. Ko, *Adv. Funct. Mater.*, 2015, **25**, 2841–2849.
53 Y. Qiu, H. P. Wu, J. Wang, J. Lou, Z. Zhang, A. P. Liu and G. Z. Chai, *J. Appl. Phys.*, 2018, **123**, 084103.
54 Y. Qiu, H. P. Wu, J. Wang, J. Lou, Z. Zhang, A. P. Liu, T. Kitamura and G. Z. Chai, *J. Appl. Phys.*, 2017, **122**, 024103.
55 H. Wu, X. Ma, Z. Zhang, J. Zhu, J. Wang and G. Chai, *J. Appl. Phys.*, 2016, **119**, 154102.
56 H. Wu, X. Ma, Z. Zhang, J. Zeng, J. Wang and G. Chai, *AIP Adv.*, 2016, **6**, 015309.
57 Y. L. Zhao, Q. L. Liao, G. J. Zhang, Z. Zhang, Q. J. Liang, X. Q. Liao and Y. Zhang, *Nano Energy*, 2015, **11**, 719–727.
58 Y. Kim, K. Y. Lee, S. K. Hwang, C. Park, S. W. Kim and J. Cho, *Adv. Funct. Mater.*, 2014, **24**, 6262–6269.
59 J. Chun, K. Y. Lee, C. Y. Kang, M. W. Kim, S. W. Kim and J. M. Baik, *Adv. Funct. Mater.*, 2014, **24**, 2038–2043.
60 S. H. Bhang, W. S. Jang, J. Han, J. K. Yoon, W. G. La, E. Lee, Y. S. Kim, J. Y. Shin, T. J. Lee, H. K. Baik and B. S. Kim, *Adv. Funct. Mater.*, 2017, **27**, 1603497.
61 K. I. Park, S. Xu, Y. Liu, G. T. Hwang, S. J. L. Kang, Z. L. Wang and K. J. Lee, *Nano Lett.*, 2010, **10**, 4939–4943.
62 X. L. Chen, X. M. Li, J. Y. Shao, N. L. An, H. M. Tian, C. Wang, T. Y. Han, L. Wang and B. H. Lu, *Small*, 2017, **13**, 1604245.
63 S. Siddiqui, D. I. Kim, L. T. Duy, M. T. Nguyen, S. Muhammad, W. S. Yoon and N. E. Lee, *Nano Energy*, 2015, **15**, 177–185.
64 Y. Song, Y. Shen, H. Liu, Y. Lin, M. Li and C.-W. Nan, *J. Mater. Chem.*, 2012, **22**, 8063–8068.
65 Y. Park, Y.-E. Shin, J. Park, Y. Lee, M. P. Kim, Y.-R. Kim, S. Na, S. K. Ghosh and H. Ko, *ACS Nano*, 2020, **14**, 7101–7110.
66 X. H. Hu, X. Yan, L. L. Gong, F. F. Wang, Y. H. Xu, L. Feng, D. Y. Zhang and Y. G. Jiang, *ACS Appl. Mater. Interfaces*, 2019, **11**, 7379–7386.
67 Y. Zhao, Q. Liao, G. Zhang, Z. Zhang, Q. Liang, X. Liao and Y. Zhang, *Nano Energy*, 2015, **11**, 719–727.
68 Y. Mao, P. Zhao, G. McConohy, H. Yang, Y. Tong and X. Wang, *Adv. Energy Mater.*, 2014, **4**, 1301624.
69 Y. Zhang, M. Wu, Q. Zhu, F. Wang, H. Su, H. Li, C. Diao, H. Zheng, Y. Wu and Z. L. Wang, *Adv. Funct. Mater.*, 2019, **29**, 1904259.
70 K. Breuer, *Nature*, 2019, **570**, 448–449.
71 D. Floreano and R. J. Wood, *Nature*, 2015, **521**, 460–466.
72 N. T. Jafferis, E. F. Helbling, M. Karpelson and R. J. Wood, *Nature*, 2019, **570**, 491–495.
73 N. Savage, *Nature*, 2015, **521**, S64–S65.
74 K. Y. Ma, P. Chirarattananon, S. B. Fuller and R. J. Wood, *Science*, 2013, **340**, 603–607.
75 Y. Chen, H. Wang, E. F. Helbling, N. T. Jafferis, R. Zufferey, A. Ong, K. Ma, N. Gravish, P. Chirarattananon, M. Kovac and R. J. Wood, *Sci. Robot.*, 2017, **2**, eaao5619.
76 Y. Chen, H. Zhao, J. Mao, P. Chirarattananon, E. F. Helbling, N.-S. P. Hyun, D. R. Clarke and R. J. Wood, *Nature*, 2019, **575**, 324–329.

